

3D Flow Field Estimation and Assessment for Live Cell Fluorescence Microscopy - Supplementary Material

Sandeep Manandhar¹, Patrick Bouthemy¹, Erik Welf², Gaudenz
Danuser², Philippe Roudot², and Charles Kervrann¹

¹Inria, Centre Rennes-Bretagne Atlantique, 35042, France

²Lyda Hill Department of Bioinformatics, UTSouthwestern, Dallas,
Texas, 75390, USA

1 3D Census signature-based Optical Flow

In this section, we briefly describe the integration of the Census signature (CS) in the variational setting.

First, we recall that a bit of the CS is a binarized form of image derivative, given as:

$$H(r) = \begin{cases} 0, & \text{if } |r| \geq 0 \\ 1 & \text{otherwise,} \end{cases} \quad (1)$$

where $r = I_1(\mathbf{p}) - I_2(\mathbf{q})$ and \mathbf{q} belongs to the neighbourhood $\mathcal{N}(\mathbf{p})$ of \mathbf{p} . To form the CS of \mathbf{p} , all \mathbf{q} 's in its neighbourhood has to be considered, and their binarized derivatives have to be ordered in a given order.

Instead of binary bits, we assign continuous values to the directional derivatives, and we call a directional derivative, a Census element of the CS. One can note that $H(r)$ is a step function.

Following Hafner et al.¹ approximate the step function with a smoother version as :

$$H_\epsilon(r) = \frac{1}{2} \left(1 + \frac{r}{\sqrt{r^2 + \epsilon^2}} \right), \quad (2)$$

and its first-order derivative is then given by:

$$H'_\epsilon(r) = \frac{\epsilon^2}{2(r^2 + \epsilon^2)^{3/2}}, \quad (3)$$

¹Hafner, Demetz, and Weickert, *Why is the Census Transform Good for Robust Optic Flow Computation?*, 2013.

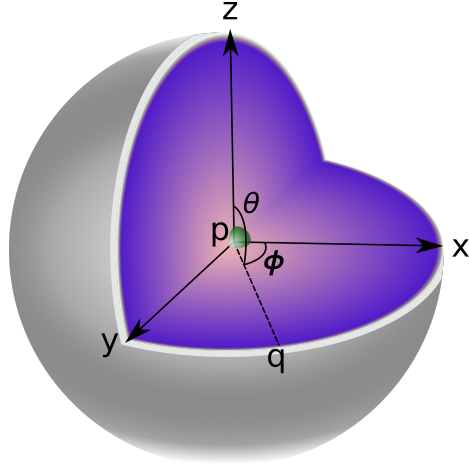


Figure 1: Continuous CS. Here \mathbf{p} is the central voxel. The Census bit is computed for its neighbour \mathbf{q} which lies at the spherical coordinates of $(1, \theta, \phi)$, as specified by the directional derivative operator ∂_ϕ^θ .

where ϵ is the step-function approximation factor. In what follows, $r = \partial_\phi^\theta I(\mathbf{p})$, where ∂_ϕ^θ acts as a spatial directional derivative operator with direction specified by the spherical angles, (ϕ, θ) , with $\theta \in [0, \pi]$ and $\phi \in [0, 2\pi)$, in a unit sphere around central voxel \mathbf{p} , as illustrated in Fig. 1. Let the unit 3D sphere centered at \mathbf{p} be denoted as $\mathbb{S}^2(\mathbf{p}, 1)$, which is a (n-1)-sphere (the sphere defined by the set of points precisely on the sphere and not inside of it). Now, any $\mathbf{q} \in \mathbb{S}^2(\mathbf{p}, 1)$ can be parameterized by $(1, \phi, \theta)$.

In continuous setting, the Census elements are computed for all $\mathbf{q} \in \mathbb{S}^2(\mathbf{p}, 1)$ in the unit sphere which results in the continuous CS of infinite length. Practically, the values of ϕ and θ are discretized to obtain CS of finite length.

1.1 Definition of CS is the Variational Framework

1.1.1 Data term modeling

In order to put the Census signature constancy assumption into the perspective of data term for the variational optical flow method, we take a pair of corresponding points $(x, y, z, t)^\top$ and $(x + u, y + v, z + w, t + 1)^\top$ from two volume pairs, I_t and I_{t+1} . Let $\mathbf{w} = (u, v, w, 1)^\top$ be the motion vector to be estimated. For the sake of brevity, we denote the space and time coordinates together as quadruplets $\mathbf{p} = (x, y, z, t)^\top$. According to the constancy assumption of the CS we have, for all pairs of (ϕ, θ) ,

$$H_\epsilon(\partial_\phi^\theta I_{t+1}(\mathbf{p} + \mathbf{w})) - H_\epsilon(\partial_\phi^\theta I_t(\mathbf{p})) \sim 0. \quad (4)$$

We linearize 4 in two stages. First, $\partial_\phi^\theta I(\mathbf{x} + \mathbf{w})$ is linearized with respect to \mathbf{x} , as:

$$\partial_\phi^\theta I(\mathbf{p} + \mathbf{w}) = \partial_\phi^\theta I(\mathbf{p}) + \mathbf{w}^\top \nabla(\partial_\phi^\theta I(\mathbf{p})), \quad (5)$$

$$H_\epsilon(\partial_\phi^\theta I(\mathbf{p}) + \mathbf{w}^\top \nabla(\partial_\phi^\theta I(\mathbf{p}))) - H_\epsilon(\partial_\phi^\theta I(\mathbf{p})) \sim 0, \quad (6)$$

with ∇ as a spatio-temporal gradient operator. Finally, we linearize H_ϵ with respect to $\partial_\phi^\theta(I(\mathbf{x}))$ using first order Taylor series expansion as,

$$H_\epsilon(\partial_\phi^\theta I(\mathbf{p}) + \mathbf{w}^\top \nabla(\partial_\phi^\theta I(\mathbf{p}))) = H_\epsilon(\partial_\phi^\theta I(\mathbf{p})) + H'_\epsilon(\partial_\phi^\theta I(\mathbf{p})).\mathbf{w}^\top \nabla(\partial_\phi^\theta I(\mathbf{p})). \quad (7)$$

From eqs. 6 and 7, we come up with:

$$H'_\epsilon(\partial_\phi^\theta I(\mathbf{p})).\mathbf{w}^\top \nabla(\partial_\phi^\theta I(\mathbf{p})) \sim 0. \quad (8)$$

The sum of elements on the left-hand side of Eq. 8, for every $(1, \phi, \theta)$ approximates the equivalent Hamming distance. Now, we create the data term based on the Census constancy assumption using Eq. 8 as:

$$D(I, \mathbf{w}) = \int_0^{2\pi} \int_0^\pi H'_\epsilon(\partial_\phi^\theta I(\mathbf{p})).(\mathbf{w}^\top \nabla(\partial_\phi^\theta I(\mathbf{p}))) d\theta d\phi. \quad (9)$$

1.1.2 Variational Energy Form

We use quadratic norm for both the data and the regularization terms to make the solution tractable. We write this energy functional as:

$$E(\mathbf{w}) = \int_\Omega \|D(I, \mathbf{w})\|_2^2 + \alpha \|\nabla \mathbf{w}\|_2^2 d\mathbf{p}, \quad (10)$$

where $\mathbf{p} \in \Omega$, α is a smoothing parameter and ∇ is a gradient operator and the function D is given as:

$$D(I(\mathbf{p}), \mathbf{w}(\mathbf{p})) = \int_0^{2\pi} \int_0^\pi H_\epsilon'^2(\partial_\phi^\theta I(\mathbf{p})).(\mathbf{w}(\mathbf{p})^\top \nabla(\partial_\phi^\theta I(\mathbf{p})))^2 d\theta d\phi, \quad (11)$$

Minimizers u, v, w (i.e., the components of \mathbf{w}) of Eq. 10 can be found by solving the associated Euler-Lagrange (E.L.) equations. For the sake of brevity, we remove limits from the integration sign and \mathbf{p} argument from the function I , to write the E.L. equations as:

$$\int \int H_\epsilon'^2(\partial_\phi^\theta I) \partial_\phi^\theta I_x . \mathbf{w}^\top \nabla(\partial_\phi^\theta I) d\theta d\phi - \alpha \Delta u = 0, \quad (12)$$

$$\int \int H_\epsilon'^2(\partial_\phi^\theta I) \partial_\phi^\theta I_y . \mathbf{w}^\top \nabla(\partial_\phi^\theta I) d\theta d\phi - \alpha \Delta v = 0, \quad (13)$$

$$\int \int H_\epsilon'^2(\partial_\phi^\theta I) \partial_\phi^\theta I_z . \mathbf{w}^\top \nabla(\partial_\phi^\theta I) d\theta d\phi - \alpha \Delta w = 0, \quad (14)$$

where I_x, I_y and I_z denote the intensity gradients.

1.2 Implementation

The integrals in eqs. 12, 13, 14 are approximated by discrete summation over fixed site cliques. Here, we consider a 26-connected neighbourhood. Let \mathcal{N} denote the neighbourhood of voxel i , $|\mathcal{N}| = N$, and j the n^{th} neighbour. In what follows, $\partial_n I$ denotes the directional derivative in the discrete setting and given as:

$$\partial_n I_{i,j} = I(j) - I(i). \quad (15)$$

We write the double integral terms of Eq. 12 to solve for u (similarly for eqs. 13 and 14 to solve for v and w , respectively) as:

$$A_x(f, \mathbf{w}) = \frac{2}{N} \sum_{n=0}^{N-1} H'_\epsilon{}^2(\partial_n I) \partial_n I_{x \cdot \mathbf{w}}^\top \nabla(\partial_n I). \quad (16)$$

These equations can be solved iteratively, using successive over-relaxation. We briefly, show the steps involved. Let,

$$B_{ix}^n = H'_\epsilon{}^2(\partial_n I(i)) \partial_n I_x, \quad (17)$$

$$S_i^u = \sum_{l \in (x,y,z)} \left(\sum_{j \in \mathcal{N}_l^-(i)} u_j^{k+1} + \sum_{j \in \mathcal{N}_l^+(i)} u_j^k \right), \quad (18)$$

$$S_i^v = \sum_{l \in (x,y,z)} \left(\sum_{j \in \mathcal{N}_l^-(i)} v_j^{k+1} + \sum_{j \in \mathcal{N}_l^+(i)} v_j^k \right), \quad (19)$$

$$S_i^w = \sum_{l \in (x,y,z)} \left(\sum_{j \in \mathcal{N}_l^-(i)} w_j^{k+1} + \sum_{j \in \mathcal{N}_l^+(i)} w_j^k \right), \quad (20)$$

where, $\mathcal{N}_l^-(i)$ and $\mathcal{N}_l^+(i)$ are causal and non causal neighbourhood of i while considering a raster scan order, and k is the number of iterations. Now, we solve for scalar component u of the motion field at i location as:

$$u_i^{k+1} = (1 - \omega) u_i^{k+1} - \omega \frac{\frac{2}{N} \sum_{n=0}^{N-1} B_{ix}^n \left(v_i^k \frac{\partial}{\partial y} \partial_n I(i) + w_i^k \frac{\partial}{\partial z} \partial_n I(i) + \frac{\partial}{\partial t} \partial_n I(i) \right) + \alpha S_i^u}{\frac{2}{N} \sum_{n=0}^{N-1} B_{ix}^n \frac{\partial}{\partial x} \partial_n I(i)}, \quad (21)$$

where $\omega \in [1, 2]$ is the relaxation parameter. Using the updated scalar field of

u , we solve for the scalar fields v and then w .

$$v_i^{k+1} = (1 - \omega)v_i^{k+1} - \omega \frac{\frac{2}{N} \sum_{n=0}^{N-1} B_{iy}^n \left(u_i^{k+1} \frac{\partial}{\partial x} \partial_n I(i) + w_i^k \frac{\partial}{\partial z} \partial_n I(i) + \frac{\partial}{\partial t} \partial_n I(i) \right) + \alpha S_i^v}{\frac{2}{N} \sum_{n=0}^{N-1} B_{iy}^n \frac{\partial}{\partial y} \partial_n I(i)}, \quad (22)$$

$$w_i^{k+1} = (1 - \omega)w_i^{k+1} - \omega \frac{\frac{2}{N} \sum_{n=0}^{N-1} B_{iz}^n \left(u_i^{k+1} \frac{\partial}{\partial x} \partial_n I(i) + v_i^{k+1} \frac{\partial}{\partial y} \partial_n I(i) + \frac{\partial}{\partial t} \partial_n I(i) \right) + \alpha S_i^w}{\frac{2}{N} \sum_{n=0}^{N-1} B_{iz}^n \frac{\partial}{\partial z} \partial_n I(i)}. \quad (23)$$

2 Comparison of Methods

2.1 Generated Flow Fields

Here, we present the 3PHS map of the generated flow fields. Figures 2, 3, and 4 depict the ground truth flow field, and the computed flow fields using Amat's method and our method, respectively.

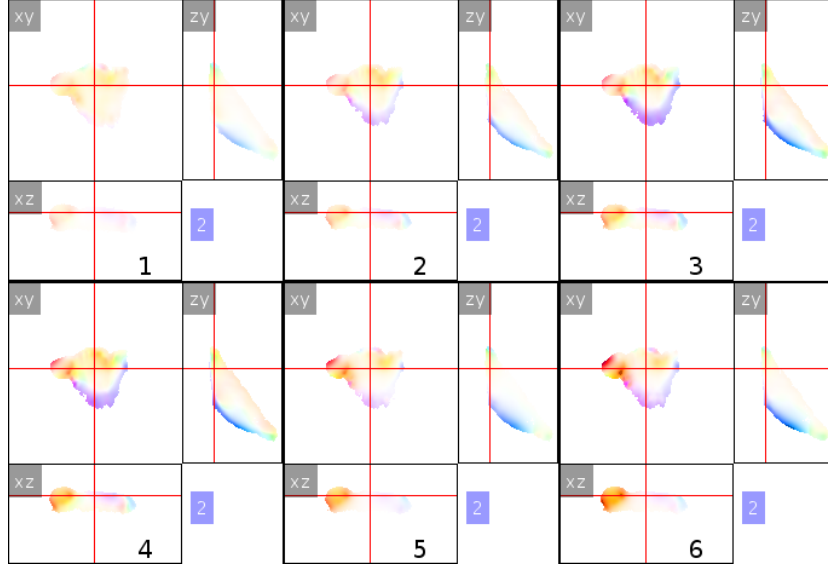


Figure 2: 3PHS map of ground truth flow fields. The saturation level has been normalized with 2 unit of motion magnitude.

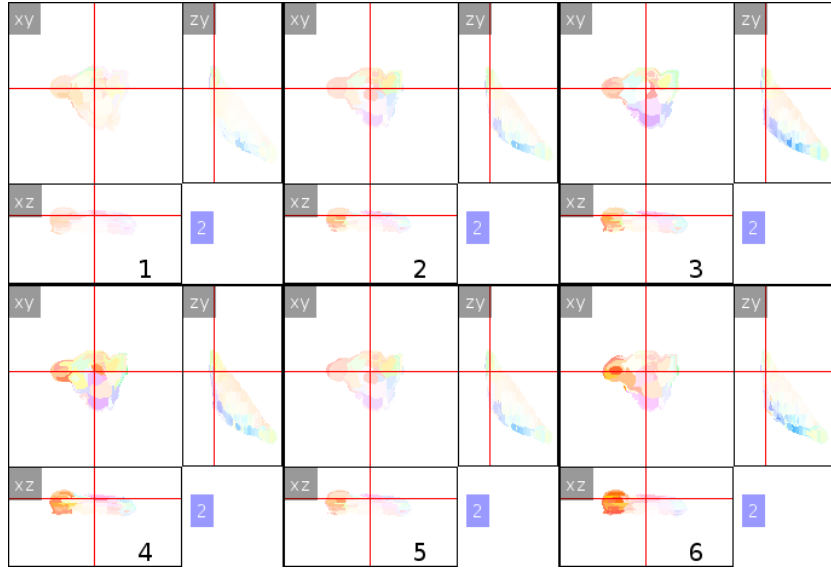


Figure 3: 3PHS map of flow fields computed using Amat's method. The saturation level has been normalized with 2 unit of motion magnitude.

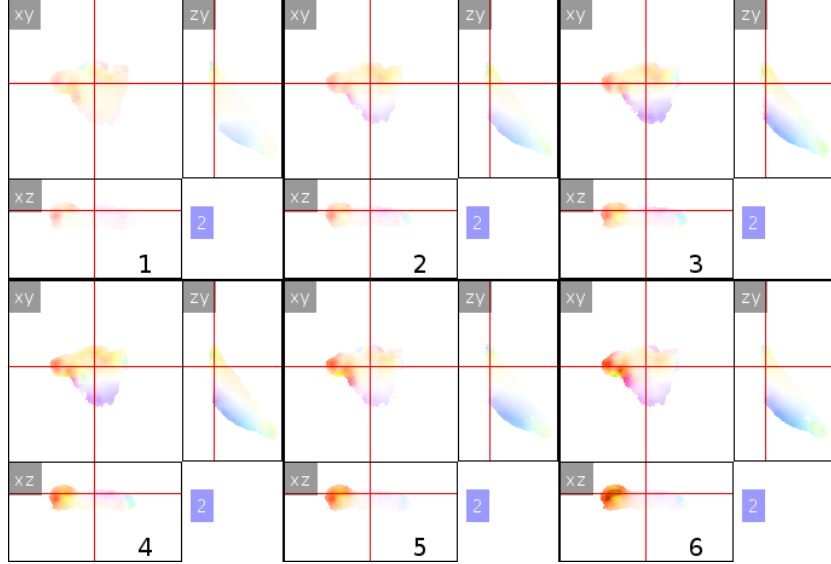
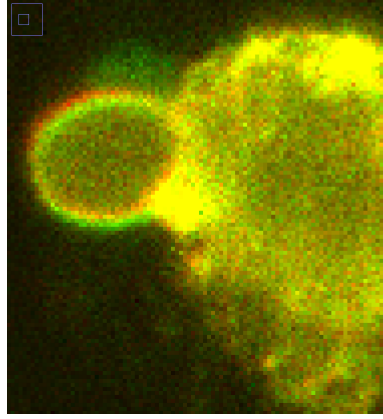


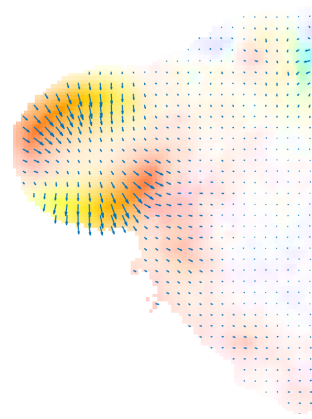
Figure 4: 3PHS map of flow fields computed using our method. The saturation level has been normalized with 2 unit of motion magnitude.

2.2 Sequence 1

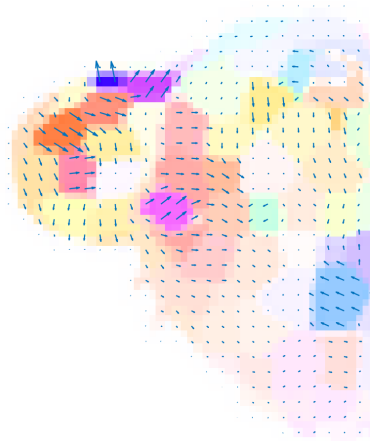
Here, we further elaborate on the comparison in Fig. 7 of the main paper. To demonstrate the effectiveness of our method, we now overlay arrow plot on our 3PHS map in Fig. 5. Upon visual inspection, it is clear that the bleb shows small displacement towards the bottom-right direction in the xy -plane. The flow fields computed by our method and Amat’s method convey the direction. Meanwhile, the flow field computed with 3D Horn-and-Schunck shows inconsistent motion on the upper side of the bleb, which moves slightly towards the upper-right direction in the xy -plane.



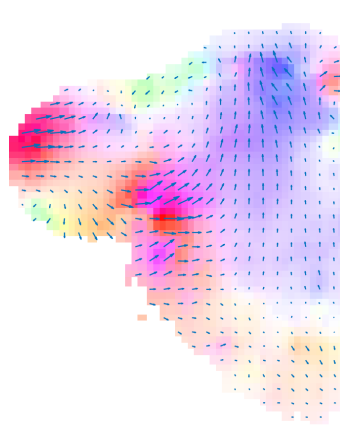
(a) Overlay of source in magenta, target in green



(b) Result obtained with our method



(c) Result obtained with Amat’s method



(d) Result obtained with 3D Horn-and-Schunck method

Figure 5: Zoomed version of Fig. 7 in the main paper. Arrows overlaid on the xy -plane of 3PHS map.

Table 1: Mean and Median of ASAE in the cytosol and the filopodium regions in Sequence 2.

| Region | Amat’s method | | Our method | |
|------------|---------------|--------|------------|--------|
| | Mean | Median | Mean | Median |
| Cytosol | 0.27 | 0.13 | 0.37 | 0.17 |
| Filopodium | 0.428 | 0.15 | 0.153 | 0.107 |

2.3 Sequence 2

Here, we display the SAE map for the cell channel of Sequence 2. Figure 6 depicts the SAE as heat map. The principal orientation of the structures in the image has be visualized with arrows overlaid on the SAE map. Clearly, the SAE maps demonstrate that our optical flow method outperforms Amat’s one. However, the SAE measure tends to be higher in the larger region of cytosol for both methods. Practically, this region is of less importance for the biological study as no (fluorescence) labeling was applied there. In contrast, the dynamics of Filopodium motion is of key biological interest. Because of higher errors in the larger cytosol region for both methods, the two global ASAE increase and are finally close to each other (gap of 0.04), hiding the difference of performance between our method and Amats method on the Filopodium part. We have reported mean and median of SAE in Cytosol and Filopodium regions for both methods in Table 1 of the supplementary document.

3 Video Description

Videos of the results can be downloaded here:

<http://serpico.rennes.inria.fr/doku.php?id=data:index>

Remark: In the video frames, left-hand panel shows the volume at time T and the right-hand panel shows the flow field computed for volume pair at T and $T + 1$. However, the last video frame shows the volume at time $T + 1$ with the flow field computed for pair at T and $T + 1$. This was done to avoid blank right-hand panel.

3.1 Sequence 1

Sequence 1 is composed of 23 volume frames of a MV3 cell undergoing blebbing. In the 3PHS rendering (see the main article for the description), left-hand side of the frame shows the orthogonal planes taken at point (128, 128, 29) in the source volume. The right-hand side shows the respective color coded flow fields. The flow field has been normalized to the maximum magnitude of the 3D flow field of the respective frames. Normalization can be applied since there are no drastic changes in motion magnitude throughout the sequence which could possibly change the saturation between frames, and make the rendering unintelligible over time.

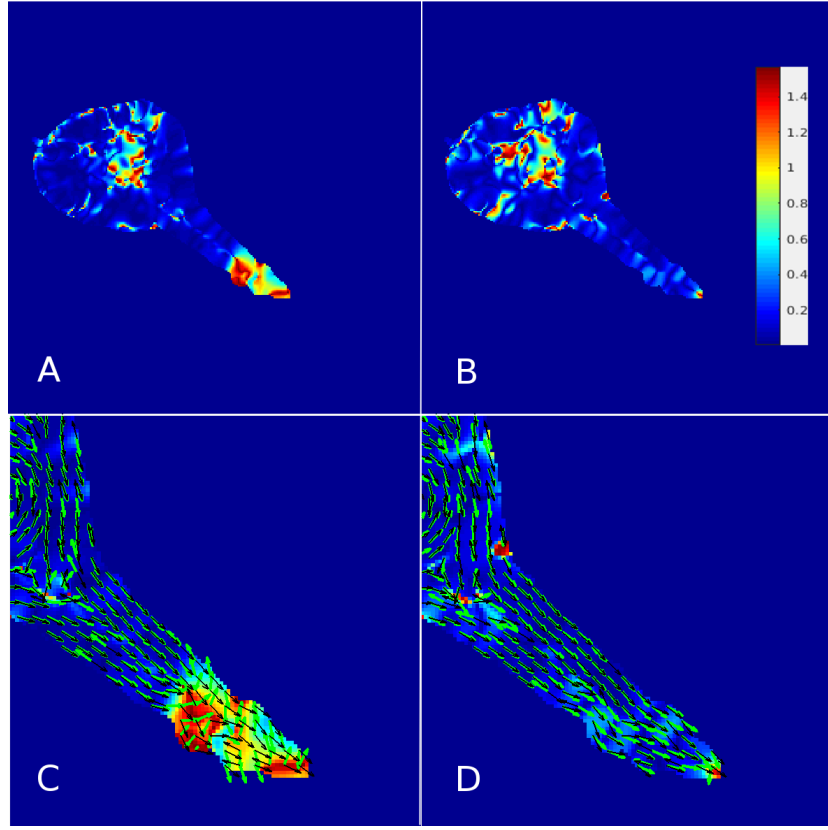
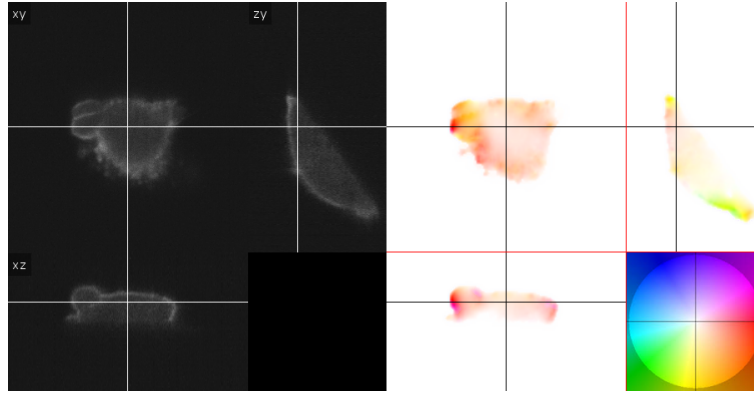


Figure 6: SAE map for the optical flow computed with (A) Amat's method (B) Our method. The color code is given in the right side of (B). Principal orientation of the structures denoted by arrows in black for original source volume, and in green for reconstructed source volume by the optical flow computed using (C) Amat's method and (D) Our method.

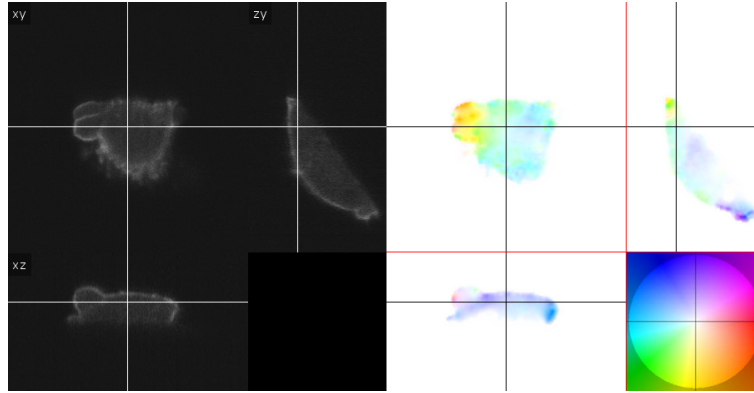
The motion of bleb is consistently rendered with the color code. The smoothness of the motion between frames can be visualized throughout the sequence except for the time frames between the 6th and the 11th. During this interval, changes in global motion can be observed (more pronounced in xy plane). These changes could have been induced by the vibration in the acquisition setup. Our rendering shows these abrupt changes in the global motion as well (see Fig. 7).

3.2 Sequence 2 (Cell)

Sequence 2, is composed of three volume frames of a MV3 cell undergoing large scale retraction in a collagen environment. The volumes are subset (time frame 11,12,13) of a longer sequence and the only interesting ones for us in order



(a) 6th-7th frames



(b) 7th-8th frames

Figure 7: 3PHS flow visualization between two frames of Sequence 1

to demonstrate large displacements. In the 3PHS rendering, left-hand side of the frame shows the orthogonal projections taken at point $(216, 256, 46)$ in the source volume. The right-hand side shows the respective color-coded flow fields. The flow field has been normalized to 50 units of motion magnitude (see Fig. 8).

3.3 Sequence 2 (Collagen)

We present three volume frames depicting collagen activity during the large scale retraction of the MV3 cell. The volumes are subset (frames 11,12,13) of a longer sequence and the interesting ones for us in order to simultaneously exhibit large and small displacements. In the 3PHS rendering, left-hand side of the frame shows the orthogonal projections taken at point $(236, 256, 45)$ in the source volume. The right-hand side shows the respective color coded flow fields. There are small and large displacements present within a frame and throughout

Table 2: ASAE of the optical flow computed with Amat’s method and our method in Sequence 3.

| Pair # | Amat’s method | Our method |
|--------|---------------|------------|
| 1 | 0.352 | 0.2638 |
| 2 | 0.2266 | 0.2254 |
| 3 | 0.2222 | 0.2206 |

the sequence. The flow field has been normalized to 3 units of motion magnitude to keep the lower saturation level within a limit such that both small and large motion types can be appreciated in the rendering (see Fig. 9). This comes at the cost of larger displacements being rendered in over saturated level. This is a compromise we have to make in order to visualize both types of motion in one rendering.

3.4 Additional sequence

We provide an additional sequence of collagen motion during cell migration, where we compare Amat’s method and our method. The sequence has a volume frame of size $256 \times 256 \times 101$, and contains 4 frames. The orthogonal projections and 3PHS map of the flow fields obtained by the aforementioned methods can be viewed in figs. 10, 11 and 12, respectively. The SAE measure of the computed 3D optical flow fields is reported in Table 2.

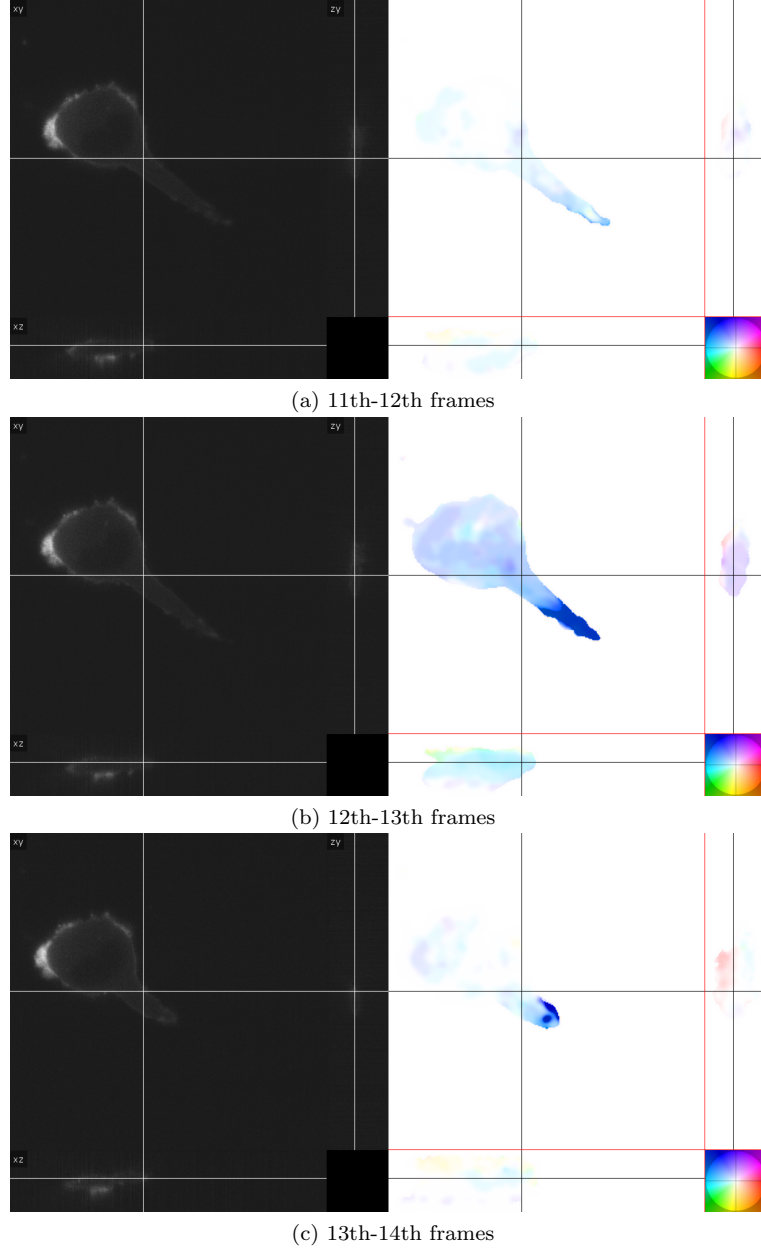
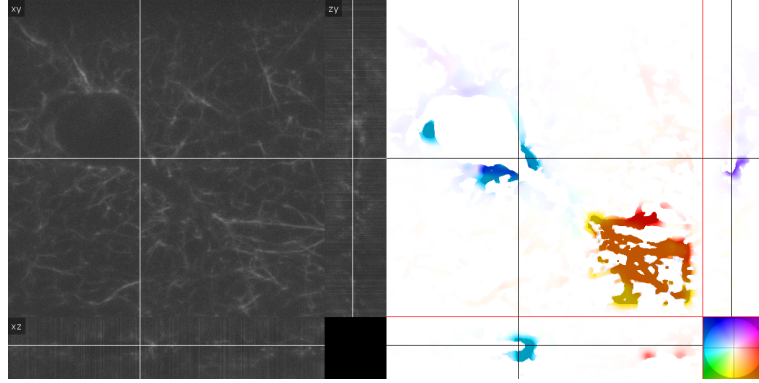
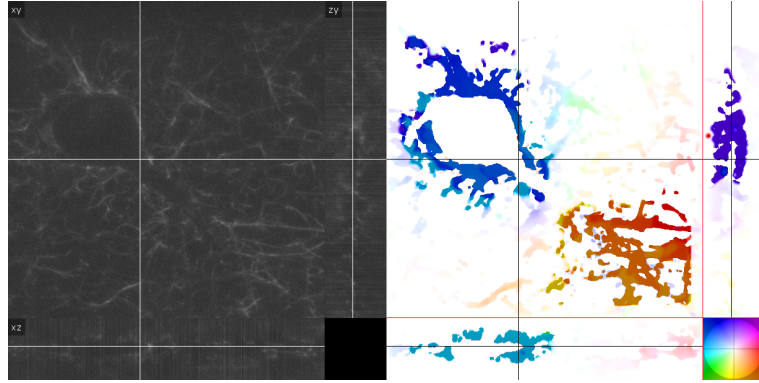


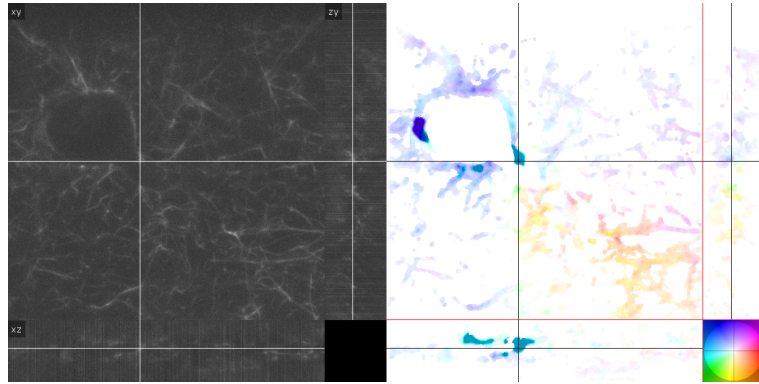
Figure 8: 3PHS flow visualization between two frames for the cell channel of Sequence 2. The color-code is given at the bottom-right corner of each figures.



(a) 11th-12th frames



(b) 12th-13th frames



(c) 13th-14th frames

Figure 9: 3PHS flow visualization between two frames for the collagen channel of Sequence 2. The color-code is given at the bottom-right corner of each figures.

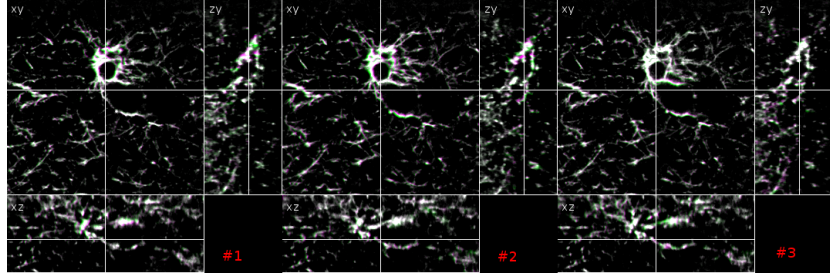


Figure 10: Additional collagen sequence.

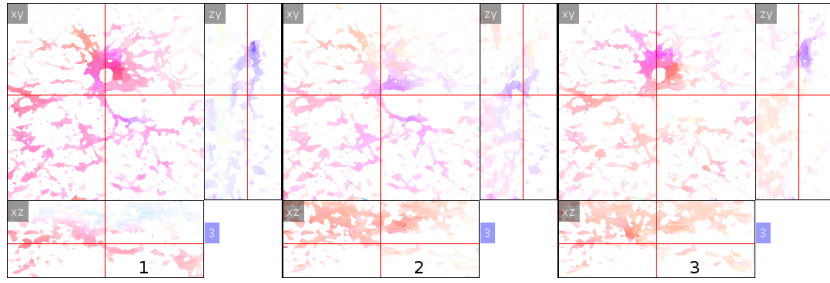


Figure 11: 3PHS map of flow field obtained with Amat's method.

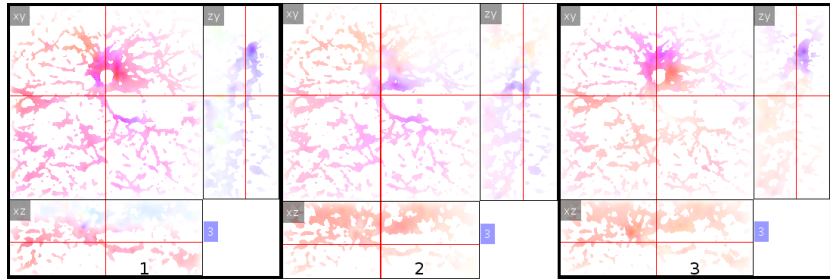


Figure 12: 3PHS map of flow field obtained with our method. One may notice the motion of thin structures being captured which is not the case with Amat's method.

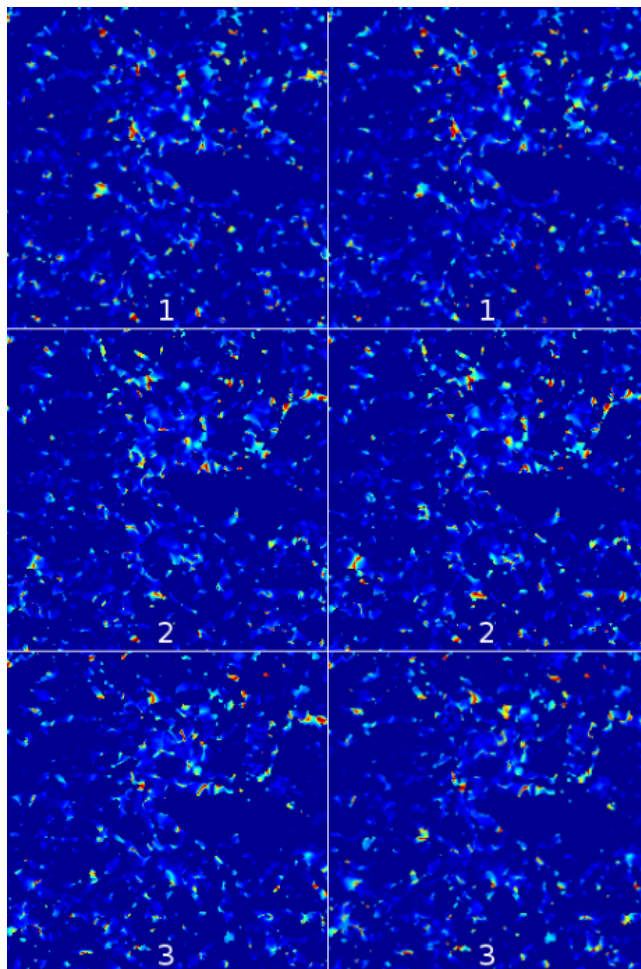


Figure 13: SAE of optical flow reconstruction for Amat's method (left) and our method (right).